Inorganic Chemistry
Article

Inorg. Chem. **2009**, *48*, 7261–7268 **7261**
DOI: 10.1021/ic9005983

SnO_2 Nanostructures-TiO_2 Nanofibers Heterostructures: Controlled Fabrication and High Photocatalytic Properties

Changhua Wang, Changlu Shao, Xintong Zhang, and Yichun Liu*

Center for Advanced Optoelectronic Functional Materials Research, Key Laboratory for UV Light-Emitting Materials and Technology of Ministry of Education, Northeast Normal University, Changchun 130024, People's Republic of China

Received March 27, 2009

Combining the versatility of the electrospinning technique and hydrothermal growth of nanostructures enabled the fabrication of hierarchical SnO_2/TiO_2 composite nanostructures. The results revealed that not only were secondary SnO_2 nanostructures successfully grown on primary TiO_2 nanofiber substrates but also the SnO_2 nanostructures were uniformly distributed without aggregation on TiO_2 nanofibers. By adjusting fabrication parameters, the morphology as well as coverage density of secondary SnO_2 nanostructures could be further controlled, and then SnO_2/TiO_2 heterostructures with SnO_2 nanoparticles or nanorods were facilely fabricated. The photocatalytic studies suggested that the SnO_2/TiO_2 heterostructures showed enhanced photocatalytic efficiency of photodegradation of Rhodamine B (RB) compared with the bare TiO_2 nanofibers under UV light irradiation.

1. Introduction

TiO_2 has been well-known as an excellent photocatalytic material which can find applications in various fields including water splitting, environmental purification, self-cleaning and superhydrophilic surfaces, sensors, and disinfection.[1−6] However, enhancing the photocatalytic efficiency of TiO_2 to meet the practical application requirements is still a challenge because of the bottleneck of poor quantum yield caused by the rapid recombination of photogenerated electrons and holes. Much effort has been made to increase the electron−hole pair separation efficiency. Therein, TiO_2 based homostructure and heterostructure such as anatase/rutile homostructure,[7] noble metal (Ag,[8] Au,[9] Pt,[10] Pd,[11] etc.)/TiO_2, carbon (nanotube,[12] nanowall,[13] nanofiber,[14] graphene,[15] etc.) /TiO_2, M_xO_y (ZnO,[16] SnO_2,[17] etc.)/TiO_2 and M_xS_y (CdS,[18] PbS,[19] etc.)/TiO_2 heterostructures have received the most attention recently because of their excellent catalytic activity. Among the semiconductor/TiO_2 systems, SnO_2/TiO_2 heterostructure attracts much interest in particular because of their structural analogy. That is, both oxides TiO_2 and SnO_2 belong to the same crystal symmetry (tetragonal) and have two molecular units per primitive unit cell ($Z = 2$).[20] Additionally, the band gap of SnO_2 (Eg = 3.5−3.6 eV) is higher than that of TiO_2 (Eg = 3.0 eV for rutile, Eg = 3.2 eV for anatase), but the conduction band (CB) of SnO_2 (E_{CB} for SnO_2 = 0 V versus NHE at pH 7) is lower than that of TiO_2 (E_{CB} for TiO_2 = −0.5 V versus NHE at pH 7). As a consequence, in the SnO_2/TiO_2 heterostructure, the interface between SnO_2 and TiO_2 is a "type II heterojunction", meaning that the valence band (VB) of TiO_2 is positioned (energetically) between the VB and CB of SnO_2, and the CB of TiO_2 is positioned above the VB and CB of SnO_2.

*To whom correspondence should be addressed. E-mail: ycliu@nenu.edu.cn. Phone: +86 431 85099168. Fax: +86 431 85684009.

(1) Fujishima, A.; Honda, K. *Nature* **1972**, *238*, 37.
(2) Thompson, T. L.; Yates, J. T., Jr. *Chem. Rev.* **2006**, *106*, 4428.
(3) Chen, X.; Mao, S. S. *Chem. Rev.* **2007**, *107*, 2891.
(4) Fujishima, A.; Zhang, X.; Tryk, D. A. *Surf. Sci. Rep.* **2008**, *63*, 515.
(5) Sun, W.; Yu, Y.; Pan, H.; Gao, X.; Chen, Q.; Peng, L. *J. Am. Chem. Soc.* **2008**, *130*, 1124.
(6) Wang, C. H.; Shao, C. L.; Liu, Y. C.; Li, X. H. *Inorg. Chem.* **2009**, *48*, 1105.
(7) Zhang, J.; Xu, Q.; Feng, Z.; Li, M.; Li, C. *Angew. Chem., Int. Ed.* **2008**, *47*, 1766.
(8) Shan, Z.; Wu, J.; Xu, F.; Huang, F.; Ding, H. *J. Phys. Chem. C* **2008**, *112*, 15423.
(9) Buso, D.; Pacifico, J.; Martucci, A.; Mulvaney, P. *Adv. Funct. Mater.* **2007**, *17*, 347.
(10) Wang, X.; Yu, J. C.; Yip, H. Y.; Wu, L.; Wong, P. K.; Lai, S. Y. *Chem.—Eur. J.* **2005**, *11*, 2997.
(11) Mohapatra, S. K.; Kondamudi, N.; Banerjee, S.; Misra, M. *Langmuir* **2008**, *24*, 11276.
(12) Yao, Y.; Li, G.; Ciston, S.; Lueptow, R. M.; Gray, K. A. *Environ. Sci. Technol.* **2008**, *42*, 4952.
(13) Wang, H.; Quan, X.; Yu, H.; Chen, S. *Carbon* **2008**, *46*, 1126.
(14) Kim, S.; Lim, S. K. *Appl. Catal. B: Environ.* **2008**, *84*, 16.
(15) Williams, G.; Seger, B.; Kamat, P. V. *ACS Nano* **2008**, *2*, 1487.
(16) Zhang, Q.; Fan, W.; Gao, L. *Appl. Catal. B: Environ.* **2007**, *76*, 168.
(17) Tada, H.; Hattori, A.; Tokihisa, Y.; Imai, K.; Tohge, N.; Ito, S. *J. Phys. Chem. B* **2000**, *104*, 4585.
(18) Banerjee, S.; Mohapatra, S. K.; Das, P. P.; Misra, M. *Chem. Mater.* **2008**, *20*, 6784.
(19) Ratanatawanate, C.; Xiong, C.; Balkus, K. J., Jr. *ACS Nano* **2008**, *2*, 1682.
(20) Hirata, T.; Ishioka, K.; Kitajima, M.; Doi, H. *Phys. Rev. B* **1996**, *53*, 8442.

Published on Web 07/09/2009

Table 1. Experimental Conditions, SnO_2 Nanostructure Characteristics, and Chemical Component of the Prepared Composite Samples

sample	$[SnCl_4]$ (mM)	temperature (°C)	morphology	crystal size (nm)	Sn/Ti ratio starting (actual[a])
TS1	0.6	150	nanoparticles	50	1:10 (1:9.90)
TS2	1.2	150	nanoparticles	70	1:5 (1:5.00)
TS3	0.6	200	nanorods	30−60 × 150−250	1:10 (1:9.78)

[a] The value is determined by EDX.

When both SnO_2 and TiO_2 are activated simultaneously, the practical implication of this "staggered" configuration of energy levels is that the CB of SnO_2 acts as a sink of photogenerated electrons. Since the photogenerated holes move in the opposite direction, they accumulate in the VB of TiO_2, and thereby hinder charge recombination and improve photocatalytic efficiency.

Besides, very recently, electrospun TiO_2 nanofibers have been the focus of research.[21−24] TiO_2 nanofibers have opened a wide spectrum of new possibilities for high photocatalytic activity and easy recovery. Moreover, the electrospun nanofibers with both high porosity and large surface area being available for reaction are promising materials for surface modification and functionalization. Motivated by the above concerns, in this work we fabricate SnO_2/TiO_2 heterostructured photocatalysts based on TiO_2 nanofibers by combining the electrospinning technique with the hydrothermal method. The adopted synthesis route ensures not only the successful growth of SnO_2 nanostructures on TiO_2 nanofibers substrate but also the high dispersion of SnO_2 nanostructures on TiO_2 nanofibers without aggregation. By simply tuning the precursor concentration or reaction temperature, we can vary the coverage density as well as the morphology of nanostructured SnO_2 (nanoparticles or nanorods), aiming at assessing the photocatalytic application potential of SnO_2/TiO_2 heterostructure. Furthermore, owing to its simple, cost-effective, and environmental-friendly process, the synthetic strategy may be fairly applicable for the synthesis of other TiO_2 nanofibers based heterostructures. Last, the photocatalytic characteristics of the as-obtained SnO_2/TiO_2 heterostructures are investigated by measuring the degradation of dye RB and compared with those of the pure electrospun TiO_2 nanofibers.

2. Experimental Section

2.1. Preparation of TiO_2 Nanofibers. One milliliter of titanium butyloxide was mixed with 1.5 mL of acetic acid and 5 mL of ethanol. Then the homogeneous solution was added to poly(vinyl pyrrolidone) (PVP) solution of about 8 wt %, followed by vigorous stirring at room temperature for 4 h. Composite PVP/titanium butyloxide nanofiber film was fabricated by electrospinning from a syringe at an applied electric voltage of 10 kV. TiO_2 nanofibers were obtained after annealing of the obtained composite nanofibers in the air at 500 °C for 12 h.

2.2. Fabrication of SnO_2/TiO_2 Heterostructures. In a typical procedure, 10 mg of the electrospun TiO_2 nanofibers were put into an autoclave containing 20 mL of $SnCl_4-H_2O-C_2H_5OH$ solution. The concentration of the $SnCl_4$ solution was fixed at 0.6 mmol L^{-1}. The pH value of the solution was adjusted to 10 by a 0.1 M NaOH aqueous solution. The autoclave was maintained at 150 °C for 12 h and then allowed to cool to room temperature. The as-fabricated products were collected out, washed with ethanol and deionized water, respectively, and then dried in an oven at 60 °C for 12 h. By this method, three samples of SnO_2/TiO_2 heterostructures were fabricated, and then were denoted as TS1, TS2, and TS3, respectively. The detailed experimental conditions were listed in Table 1. In addition, for simplicity, pure TiO_2 nanofibers were denoted as TS0.

2.3. Characterization. X-ray diffraction (XRD) patterns of the samples were recorded on a Rigaku, D/max-2500 X-ray diffractometer. Field emission scanning electron microscope (FESEM, Hitachi S-4800) was used to observe morphology of samples. Energy dispersive X-ray (EDX) spectroscopy being attached to scanning electron microscopy (SEM) was used to analyze the composition of samples. The high-resolution transmission electron microscopy (HRTEM) images were acquired using a JEOL JEM-2100 (acceleration voltage of 200 kV). X-ray photoelectron spectroscopy (XPS) was performed on a VG ESCALAB LKII instrument with Mg Kα-ADES ($h\nu$ = 1253.6 eV) source at a residual gas pressure of below 10^{-8} Pa. FT-IR spectra were obtained on Magna 560 FT-IR spectrometer. The photoluminescence (PL) spectra of photocatalysts were detected with a Jobin Yvon HR800 micro-Raman spectrometer using a 325 nm line from a He−Cd laser.

2.4. Photocatalytic Test. The photoreactor was designed with an internal light source (50 W high pressure mercury lamp with main emission wavelength 313 nm and an average light intensity of 2.85 mW cm^{-2}) surrounded by a water-cooling quartz jacket to cool the lamp, where a 100 mL of the RB solution with an initial concentration of 10 mg L^{-1} in the presence of solid catalyst (0.01 g). The solution was stirred in the dark for 30 min to obtain a good dispersion and reach adsorption−desorption equilibrium between the organic molecules and the catalyst surface. Decreases in the concentrations of dyes were analyzed by a Cary 500 UV−vis−NIR spectrophotometer at λ = 554 nm. At given intervals of illumination, the samples of the reaction solution were taken out and analyzed.

3. Results and Discussion

Figure 1a presents the SEM image of sample TS0. It can be clearly seen that the TiO_2 non-woven nanofibers are of relatively smooth surface without secondary nanostructures. The diameter of the fibers ranges from 200 to 400 nm. SEM image of the sample TS1 shown in Figure 1b indicates that there is essentially no change to the non-woven nanofibers' morphology during the growth of the SnO_2 nanoparticles. Moreover, the nanoparticles are uniformly distributed across the surface of each fiber without aggregation, offering high level exposure of the nanoparticle surface. It is worth pointing out that the high porosity and large surface area of TiO_2 non-woven nanofibers are advantageous for uniform growth and distribution of SnO_2 nanoparticles on the surface of TiO_2 nanofibers. The diameter of SnO_2 nanoparticles is about 50 nm. The EDX spectrum in Figure 1c demonstrates the

(21) Jin, M.; Zhang, X.; Nishimoto, S.; Liu, Z.; Tryk, D. A.; Emeline, A. V.; Murakami, T.; Fujishima, A. *J. Phys. Chem. C* **2007**, *111*, 658.
(22) Formo, E.; Lee, E.; Campbell, D.; Xia, Y. *Nano Lett.* **2008**, *8*, 668.
(23) Chuangchote, S.; Sagawa, T.; Yoshikawa, S. *Appl. Phys. Lett.* **2008**, *93*, 033310.
(24) Wang, N.; Sun, C.; Zhao, Y.; Zhou, S.; Chen, P.; Jiang, L. *J. Mater. Chem.* **2008**, *18*, 3909.

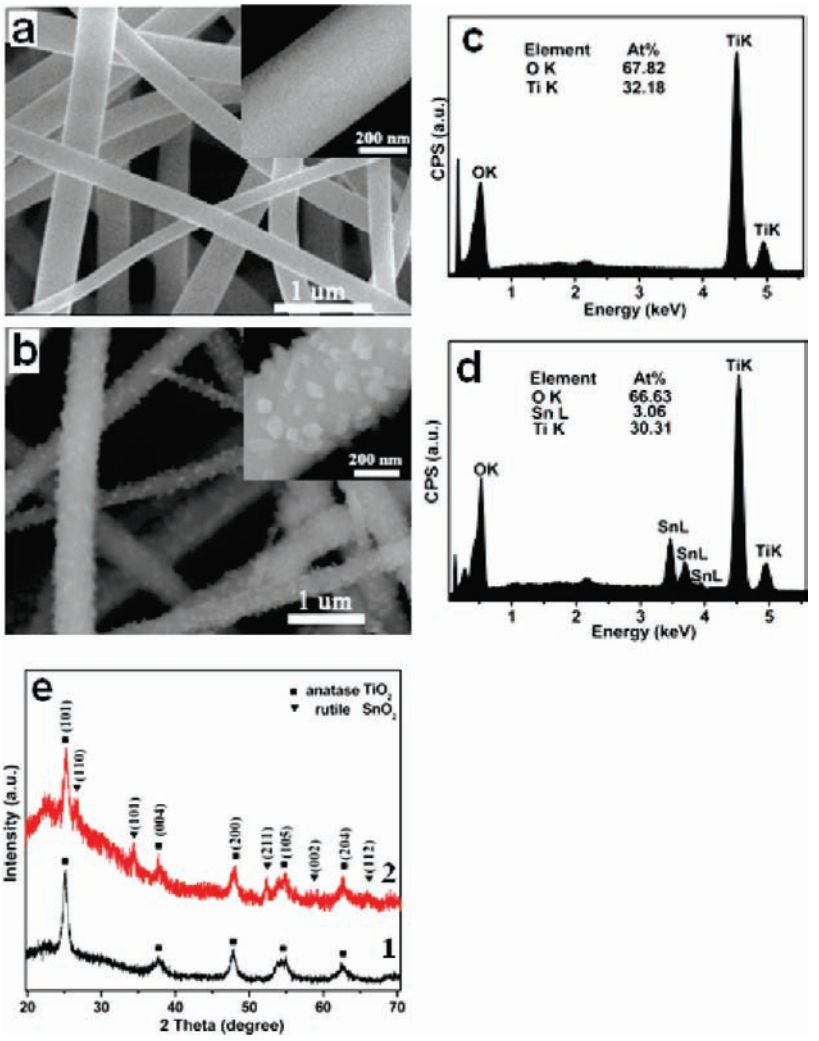

Figure 1. SEM images of sample (a) TS0 and (b) TS1; EDX spectra of sample (c) TS0 and (d) TS1; (e) XRD patterns of (1) sample TS0 and (2) TS1.

high purity of TiO_2 nanofibers. As expected, the atomic ratio of Ti to O is close to 1:2. In Figure 1d, the existence of the tin element is detected in the SnO_2/TiO_2 composite. Five different places of the SnO_2/TiO_2 heterostructures surface are analyzed by EDX, and the atomic ratio of Sn to Ti is about 1:10, confirming the uniformity of the SnO_2 nanoparticles grown on the TiO_2 nanofibers. XRD patterns of TS0 and TS1 are shown in Figure 1e. The curve 1 reveals that the crystal phase of TiO_2 nanofibers is anatase (JCPDS No. 21-1272). The curve 2 indicates that all the diffraction peaks of the SnO_2/TiO_2 heterostructures can be well indexed as rutile SnO_2 (JCPDS No. 41-1445) and the anatase TiO_2. No other impurity peaks are detected, indicating the non-existence of other impurities such as SnO, orthorhombic SnO_2, or rutile TiO_2. It is obvious that the synthesis route adopted successfully achieves SnO_2/TiO_2 heterostructure integrating the rutile phase SnO_2 with the anatase TiO_2.

TEM was used to investigate the microstructure of the sample TS1 composite in more detail. Figure 2a shows that SnO_2 nanoparticles are uniformly attached on the TiO_2 nanofibers surface, and the selected circular area is enlarged (Figure 2b). It can be observed that the diameter of SnO_2 nanoparticles is about 50 nm, which is in agreement with the SEM analysis above. A high-resolution image of the SnO_2/TiO_2 heterostructure (Figure 2c) reveals the simultaneous presence of crystalline TiO_2 and SnO_2 crystal lattices in the region of the junction. The fringes observed correspond to the interplanar distances of 0.35 and 0.26 nm, which agree well with the lattice spacing of the (101) and (101) low-index facets of the anatase TiO_2 and rutile SnO_2 crystal, respectively. Figure 2d shows the further magnified HRTEM image of the SnO_2 crystal; the measured lattice spacing of 0.26 nm can be clearly observed. These results confirm that the heterostructures are well formed between SnO_2 nanoparticles and TiO_2 nanofibers.

The chemical composition and purity of the sample TS1 composite was studied and compared with that of the sample TS0 by XPS analysis. The fully scanned spectra (Figure 3a) demonstrate that Ti, O, and C elements exist in bare TiO_2 nanofibers, while Ti, Sn, O, and C exist in SnO_2/TiO_2 heterostructures, respectively. The C element can be ascribed to the adventitious carbon-based contaminant, and the binding energy for the C1s peak at 284.6 eV is used as the reference for calibration. The high resolution XPS spectra with scanning over the following areas are analyzed: the binding energies for the Ti 2p region around 460 eV, the Sn 3d region around 490 eV, and the O 1s region around 530 eV. As shown in Figure 3b, there are two peaks in the Ti 2p region. The peak located at 464.2 eV corresponds to the Ti $2p_{1/2}$ and another one located at 458.5 eV is assigned to Ti $2p_{3/2}$. The

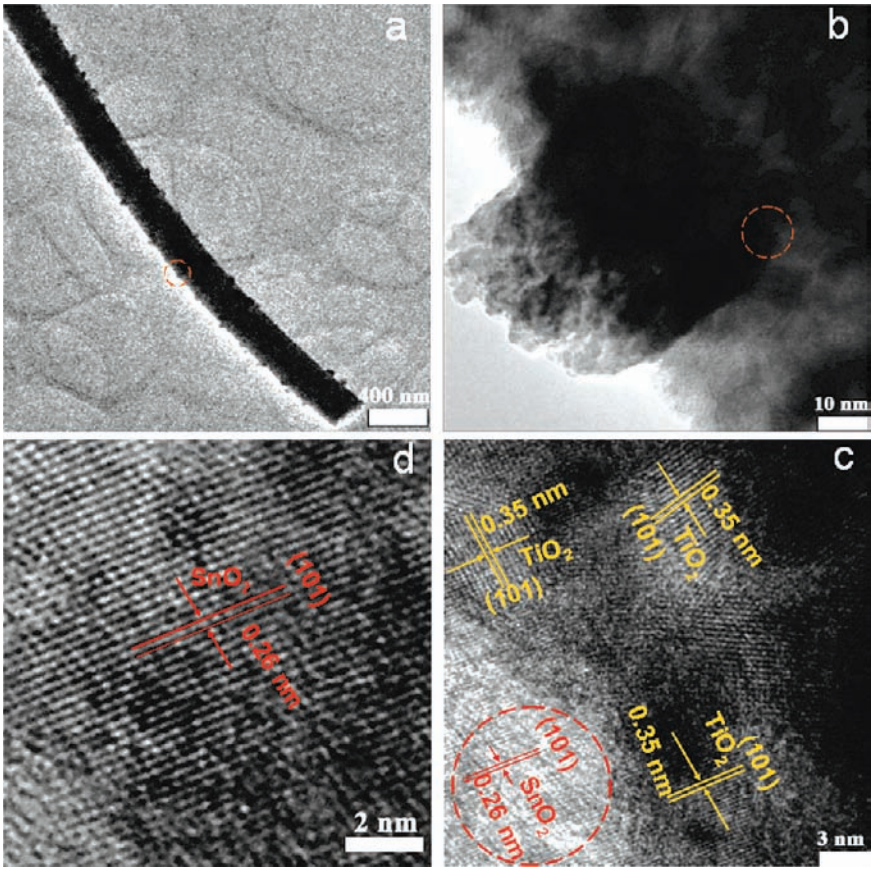

Figure 2. (a,b) TEM image of sample TS1 at different magnification. (c) HRTEM of the SnO_2/TiO_2 heterojunction region. (d) HRTEM of SnO_2 nanoparticles.

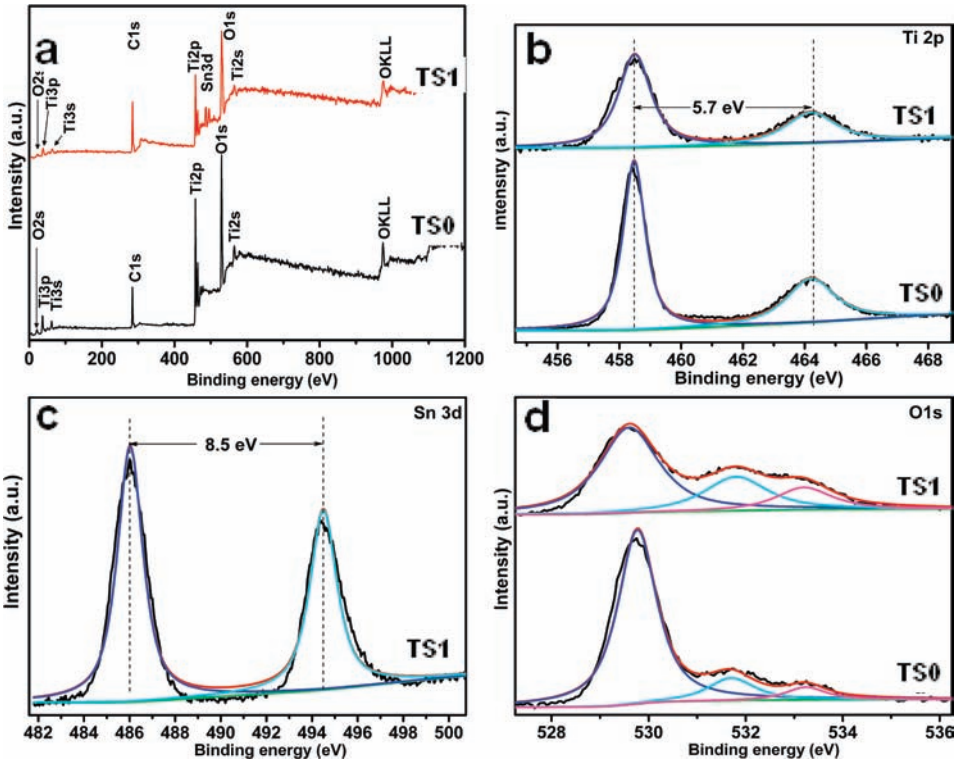

Figure 3. (a) XPS fully scanned spectra of the sample TS0 and TS1. (b) XPS spectra of Ti 2p for the sample TS0 and TS1. (c) XPS spectra of Sn 3d for the sample TS1. (d) XPS spectra of O1s for the sample TS0 and TS1.

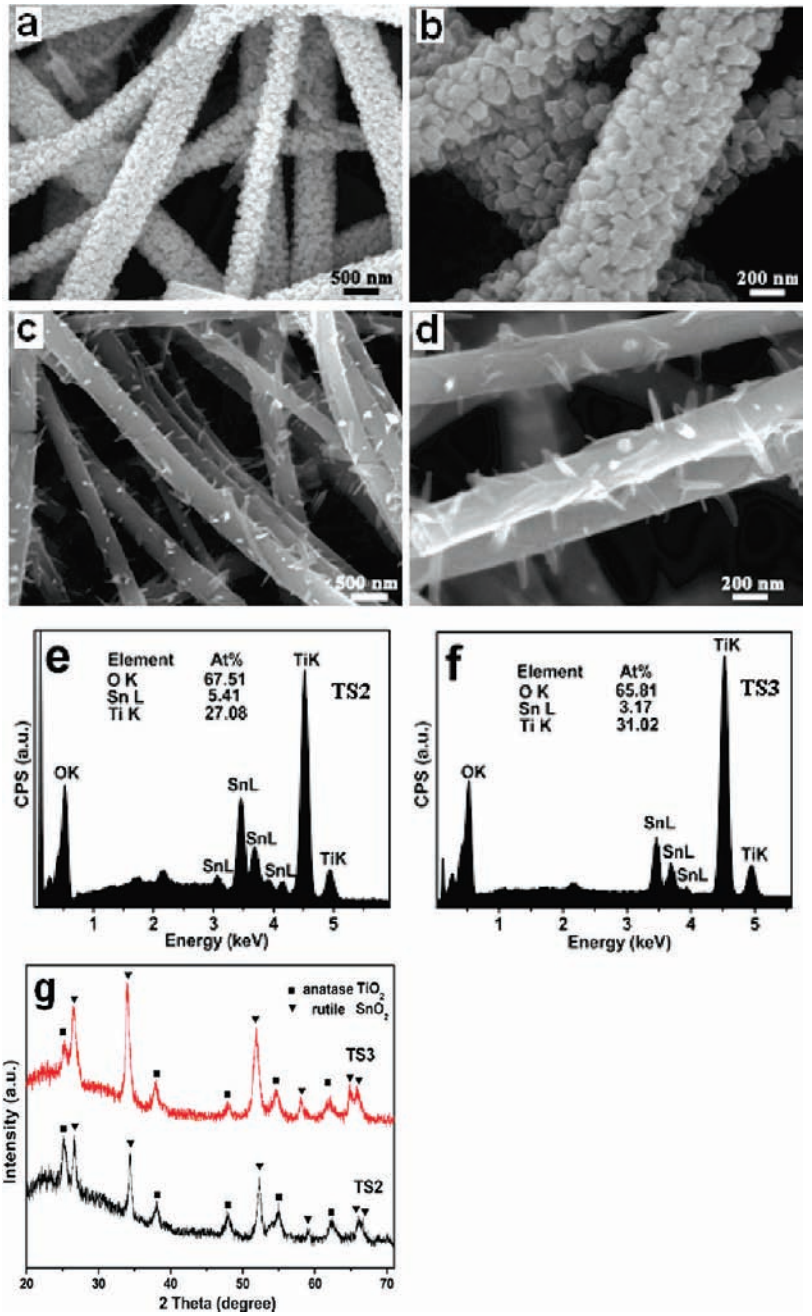

Figure 4. (a,b) SEM images of the sample TS2; (c,d) SEM images of the sample TS3; (e,f) EDX spectra of the sample TS2 and TS3; (g) XRD patterns of sample TS2 and TS3.

splitting between Ti $2p_{1/2}$ and Ti $2p_{3/2}$ is 5.7 eV, indicating a normal state of Ti^{4+} in the as-prepared SnO_2/TiO_2 heterostructures. Besides, the peaks for Ti 2p in the composite show no shift compared with that in bare TiO_2, confirming that the structure of TiO_2 remains intact after synthesis of SnO_2 nanoparticles. In Figure 3c, the Sn $3d_{5/2}$ peak is located at 486.0 eV and the Sn $3d_{3/2}$ peak is found at 494.5 eV. Moreover, the splitting of the 3d doublet of Sn is 8.5 eV, indicating that the valence state of Sn is +4. The atomic number ratio of Sn to Ti is about 0.1, as determined from our experimental XPS peak areas and their relative sensitivity factors, which is in good agreement with the EDX results above. Figure 3d presents the O 1s photoelectron peaks. The shape of a wide and asymmetric peak of O 1s spectrum indicates that there can be more than one chemical state according to the binding energy. It includes crystal lattice oxygen (O_{Ti-O} or O_{Sn-O}), surface hydroxyl groups (O_{OH}), and adsorbed water with increasing binding energy. Using the XPS Peak fitting program, version 4.1, each O 1s XPS spectrum is fitted to three kinds of chemical states. After calculation, the apparent O_{OH}/O_{Ti-O} ratio is determined to be 0.44 for the TS1 composite, which is three-times higher than that of TS0. FT-IR spectra were also further utilized to detect the surface OH groups and water adsorption on the surface of the sample (not shown). For the SnO_2/TiO_2 composite, an overlapped broad peak of high intensity at 3375 cm^{-1} is observed, which is characterized as surface Ti−OH and hydrogen-bonded molecular H_2O species. On the other hand, for the pure TiO_2 nanofibers, the intensity of the surface hydroxyl group band at 3375 cm^{-1} is significantly decreased compared with that of

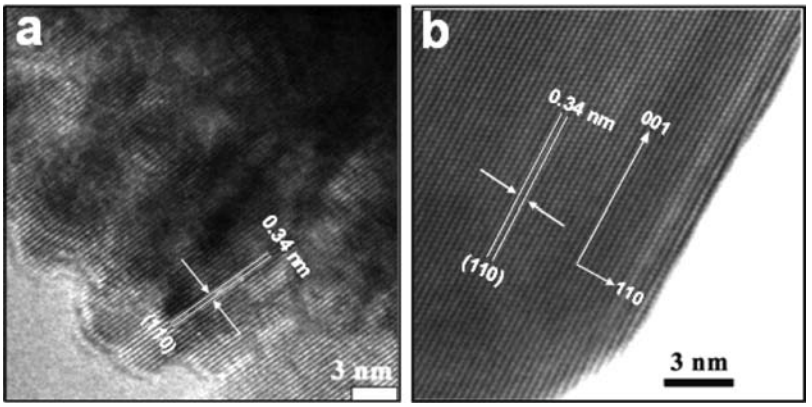

Figure 5. HRTEM images of (a) SnO_2 nanoparticles of the sample TS2 and (b) SnO_2 nanorods of the sample TS3.

the SnO_2/TiO_2 composite. Thus, it can be deduced that the amounts of surface OH groups on the surface of the composite are significantly increased by the modification of SnO_2 based on the analyses of XPS and IR. The increasing amount of surface hydroxyl group in the SnO_2/TiO_2 composite may originate from the high dispersion and hygroscopic nature of the SnO_2 nanostructure. In other words, the adsorption affinity of SnO_2 to water is much stronger than that of TiO_2. In comparison with TiO_2, SnO_2 is very sensitive to water. SnO_2 has been extensively used as a moisture sensor for this very reason.

By tuning the experimental parameters including precursor concentration and temperature, the secondary SnO_2 nanostructures grown on TiO_2 nanofibers with different density and shapes can be further controlled. Panels a and b of Figure 4 show the SEM images of the sample TS2. It can be observed that the density of the nanoparticles is dramatically increased when the precursor concentration [$SnCl_4$] is increased to 1.2 mmol L^{-1}. At the same time, the diameters of the grown nanoparticles also change from 50 to 70 nm. On the other hand, when the precursor concentration is 0.6 mmol L^{-1} and the growth temperature is increased to 200 °C, the morphology of secondary SnO_2 nanostructures grown on TiO_2 nanofibers changes significantly. Panels c and d of Figure 4 show the SEM images of the as-fabricated sample TS3. It can be observed that SnO_2 nanorods instead of nanoparticles are grown on the nanofiber substrates. The nanorods have diameters of 30−60 nm and lengths of 150−250 nm. In addition, for the as-fabricated sample TS2 and TS3, the atomic ratio of Sn to Ti is about 1:5 and 1:10, respectively, as determined by the EDX analysis (Figure 4e,f). As expected, it is in agreement with the stoichiometric composition. Figure 4g shows the XRD patterns of TS2 and TS3. The diffraction peaks indicate the SnO_2/TiO_2 composites to be a mixture of rutile SnO_2 and anatase TiO_2 phases with no other impurity phases, suggesting that neither appreciable chemical reaction between TiO_2 and SnO_2 nor anatase-to-rutile phase transition occurs during the synthesis of the SnO_2 nanostructures.

To further study the fine structures of the as-grown SnO_2 nanoparticles and nanorods, HRTEM was analyzed. The typical HRTEM images of an individual nanoparticle and nanorod are shown in Figure 5, panels a and b, respectively. Both the images reveal that the lattice spacings are 0.34 nm, which are related to the (110) plane of tetragonal rutile SnO_2. Meanwhile, Figure 5b clearly indicates that the SnO_2 nanorods are highly crystallized with few defects and grow along [001] direction. Since there is neither a template nor a surfactant in the synthesis system, it is reasonable to hypothesize that the driving forces for the growth of 1D SnO_2 nanorods come from the inherent crystal structure of SnO_2. For the rutile structure of SnO_2, the sequence of surface energy per crystal face can be described as (110) < (100) < (101) < (001) according to the calculated data.[25] Accordingly, the surfaces of (110) and (001) have the lowest and the highest surface energy, respectively, thereby the low-index (110) face is the thermodynamically most-stable bulk termination. It can properly explain the preferential growth of SnO_2 along the [001] direction in thermodynamic aspects.

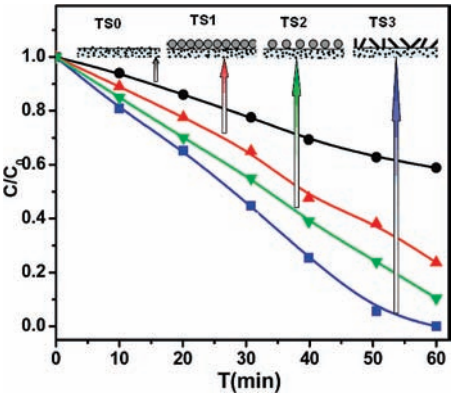

Figure 6. Curves of photocatalytic degradation of RB over different catalysts.

The photocatalytic degradation of rhodamine B has been chosen as a model reaction to evaluate the photocatalytic activities of the present SnO_2/TiO_2 heterostructures, and they are compared with that of the bare TiO_2 nanofibers. Figure 6 shows the degradation curves of RB on the SnO_2/TiO_2 heterostructures and bare TiO_2 nanofibers. In general, the SnO_2/TiO_2 heterostructures show enhanced photocatalytic activities in comparison with the bare TiO_2 nanofibers. The order of photocatalytic activities is TS3 > TS1 > TS2 > TS0.

Several reasons may account for the enhancement of the photocatalytic activity of the SnO_2/TiO_2 heterostructured photocatalyst. First, the high activity of the composite is related to the role of SnO_2 nanostructures on the surface of

(25) Leite, E. R.; Giraldi, T. R.; Pontes, F. M.; Longo, E.; Beltran, A.; Andres, J. *Appl. Phys. Lett.* **2003**, *83*, 1566.

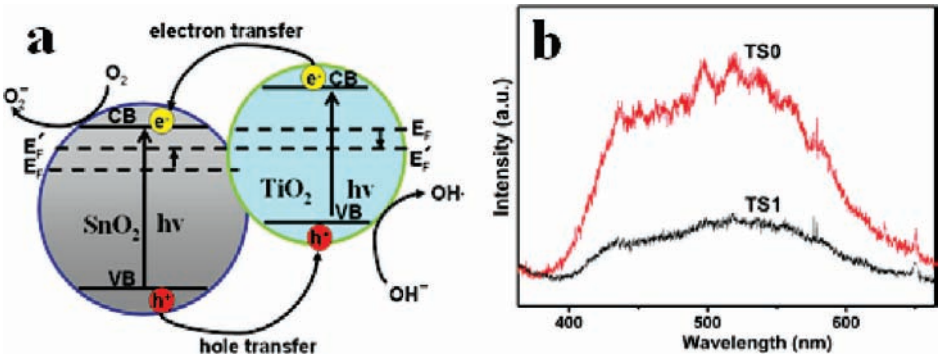

Figure 7. (a) Schematic diagram showing the energy band structure and electron−hole pair separation in the SnO_2/TiO_2 heterostructure. (b) PL emission spectra of TS0 and TS1.

TiO_2 nanofibers. A proposed mechanism for the enhanced photocatalysis of the SnO_2/TiO_2 composite is shown schematically in Figure 7a. To understand the charge transfer at the SnO_2/TiO_2 heterojunction, three relevant material properties of TiO_2 and SnO_2 including band gap, electron affinity, and work function are given. The band gap of anatase TiO_2 and rutile SnO_2 is 3.2 and 3.5 eV, respectively; the work function of TiO_2 is around 4.2 eV, its electron affinity is about 4.2 eV; the work function of SnO_2 is around 4.4 eV, its electron affinity is about 0.5 eV larger than that of TiO_2. Accordingly, a type II heterojunction is formed in the staggered arrangement at the SnO_2/TiO_2 interface. The Fermi energy level of TiO_2 is higher than that of SnO_2 because of its smaller work function, so that electron transfer occurs from the conduction band of light activated TiO_2 to the conduction band of light activated SnO_2 and, conversely, hole transfer can take place from the valence band of SnO_2 to the valence band of TiO_2. Because the Fermi level (E_F) of the semiconductor is directly related to the number of accumulated electrons, as illustrated by following: $E_F = E_{CB} + kT \ln nc/Nc$,[26] where E_{CB} is the conduction band energy, nc is the density of accumulated electrons, and Nc is the charge carrier density of the semiconductor, a negative shift in the Fermi level of the SnO_2 and a positive shift in the Fermi level of the TiO_2 would be expected. The efficient charge separation increases the lifetime of the charge carriers and enhances the efficiency of the interfacial charge transfer to adsorbed substrates, and then, account for the higher activity of the composite SnO_2/TiO_2 photocatalyst. On the contrary, in the absence of the SnO_2 nanostructures attached to the surface of the TiO_2 nanofibers, most of charges quickly recombine without doing any chemistry. Typically, only a small number of electrons (1%) and holes are trapped and participate in photocatalytic reactions, resulting in low reactivity. The better separation of electrons and holes in the SnO_2/TiO_2 heterostructures is confirmed by PL emission spectra of TS1 and TS0. (Figure 7b). It is found that TS1 exhibits much lower emission intensity than TS0, indicating that the recombination of photogenerated charge carrier is inhibited greatly in the SnO_2/TiO_2 heterostructures.

Second, the hypothetical mechanism is proposed for the photocatalytic degradation of RB as follows:

$$(SnO_2/TiO_2) + h\nu \rightarrow (SnO_2/TiO_2)(e_{CB}^- + h_{VB}+)$$

$$h^+ + OH^- \rightarrow OH\cdot$$

$$e^- + O_2 \rightarrow O_2\cdot^-$$

$$O_2\cdot^- + H_2O \rightarrow HO_2\cdot + OH^-$$

$$HO_2\cdot + H_2O \rightarrow H_2O_2 + OH\cdot$$

$$H_2O_2 \rightarrow 2OH\cdot$$

$$OH\cdot + RB \rightarrow CO_2 + H_2O$$

RB is initiated by the photoexcitation of the semiconductor system followed by the formation of the electron/hole pairs on the surface of the catalyst. Subsequent to various steps, the holes (h^+) are ultimately trapped by surface hydroxyl groups (or H_2O) at the catalyst surface to yield OH· radicals. Dissolved oxygen molecules react with conduction band electrons (e^-) to yield superoxide radical anions, $O_2\cdot^-$, which on protonation generate the hydroperoxy, $HO_2\cdot$, radicals, producing hydroxyl radical OH·, which is a strong oxidizing agent to decompose the organic dye.[27,28] An important factor for the efficient photooxidation of organic substrates will depend on the concentration of OH· radicals by photooxidation of surface hydroxyl groups and/or chemisorbed H_2O.[29] As demonstrated by XPS and IR analysis above, the amount of surface hydroxyl groups for the SnO_2/TiO_2 heterostructure is larger than that of the bare TiO_2, and thereby leads to the enhancement of the photocatalytic activity of the heterostructured SnO_2/TiO_2 nanofibers.

Then why does TS2 show considerably lower activity than TS1? Although the heterojunction favors electron flow from TiO_2 to SnO_2 nanoparticles, higher surface coverage of SnO_2 nanoparticles decreases the accessibility of the active sites of the TiO_2 nanofibers surface, and thus in turn reduces the photoactivity. Moreover, SnO_2 itself is not effective as photocatalyst, which is in agreement with the previous report

(26) Subramanian, V.; Wolf, E. E.; Kamat, P. V. *J. Am. Chem. Soc.* **2004**, *126*, 4943.

(27) Aarthi, T.; Madras, G. *Ind. Eng. Chem. Res.* **2007**, *46*, 7.

(28) Rajeshwar, K.; Osugi, M. E.; Chanmanee, W.; Chenthamarakshan, C. R.; Zanoni, M. V. B.; Kajitvichyanukul, P.; Krishnan-Ayer, R. *J. Photochem. Photobiol. C: Photochem. Rev.* **2008**, *9*, 15.

(29) Schwarz, P. F.; Turro, N. J.; Bossmann, S. H.; Braun, A. M.; Wahab, A. M. A. A.; Durr, H. *J. Phys. Chem. B* **1997**, *101*, 7127.

that TiO_2 showed high photocatalytic property while pure SnO_2 showed very low photocatalytic activity. Therefore, the photocatalytic activity of SnO_2/TiO_2 composites will decrease with the increase of SnO_2 contents when the SnO_2 content is loaded up to a certain level. Comparing the results for TS1 and TS3, which have the same composition, we suggest that the higher photocatalytic activity of the latter results from the higher crystallinity of SnO_2 nanocrystals. The higher crystallinity means fewer defects in the as-synthesized sample. It is well-known that lattice defects may act as recombination centers for photoinduced electrons and holes, thus significantly reducing the net photocatalytic activity.

4. Conclusion

The SnO_2/TiO_2 heterostructured photocatalyst have been fabricated via the electrospinning and hydrothermal methods. SEM and TEM reveal a uniform distribution of SnO_2 nanoparticles or nanorods on the TiO_2 nanofibers' surface and intimate contact between them. XPS demonstrates that there is a larger amount of surface hydroxyl groups for the SnO_2/TiO_2 composite in comparison with the bare TiO_2. The investigation of photocatalytic ability show that the SnO_2/TiO_2 composite possesses a higher photocatalytic activity than the bare TiO_2 for the degradation of RB dye under UV light irradiation because of the improvement of the separation of photogenerated electrons and holes, as well as the change of amount of surface hydroxyl groups of the catalyst. Moreover, the simple experimental procedure for the novel TiO_2/SnO_2 heterostructures is quite simple, environmentally benign, and cost-effective, permitting it to be used for the synthesis of future heterostructured photocatalysts.

Acknowledgment. This work is supported by National High Technology Research and Development Program of China (2006AA03Z311), Cultivation Fund of the Key Scientific and Technical Innovation Project (Grant 704017), Ministry of Education of China, National Natural Science Foundation of China (Grants 60576040 and 50572014), Program for New Century Excellent Talents in University (NCET-05-0322).